Received: 30 April 2024 | Accepted: 14 July 2024

DOI: 10.1002/cnl2.158

RESEARCH ARTICLE

Carbon Neutralization WILEY

Binder-induced inorganic-rich solid electrolyte interphase and physicochemical dual cross-linked network for high-performance SiO_x anode

Gang Wu[1] | Yuanhang Gao[1] | Zheng Weng[1] | Zhicheng Zheng[1] | Wenqiang Fan[1] | Anqiang Pan[1] | Ning Zhang[1] | Xiaohe Liu[1,2] | Renzhi Ma[3] | Gen Chen[1]

[1]Key Laboratory of Electronic Packaging and Advanced Functional Materials of Hunan Province, School of Materials Science and Engineering, Changsha, China

[2]School of Chemical Engineering, Zhongyuan Critical Metals Laboratory, Zhengzhou University, Zhengzhou, China

[3]International Center for Materials Nanoarchitectonics (WPI-MANA), National Institute for Materials Science (NIMS), Tsukuba, Japan

Correspondence
Anqiang Pan, Ning Zhang, Xiaohe Liu and Gen Chen, Key Laboratory of Electronic Packaging and Advanced Functional Materials of Hunan Province, School of Materials Science and Engineering, Changsha, Hunan 410083, China.
Email: pananqiang@csu.edu.cn, nzhang@csu.edu.cn, liuxiaohe@zzu.edu.cn and geenchen@csu.edu.cn

Funding information
National Natural Science Foundation of China, Grant/Award Number: 22379166; Natural Science Foundation for Distinguished Young Scholars of Hunan Province, Grant/Award Number: 2022JJ10089; Key Research and Development Program of Hunan Province, Grant/Award Number: 2023GK2015; Central South University Innovation-Driven Research Programme, Grant/Award Number: 2023CXQD034

Abstract

Silicon oxide (SiO_x) is heralded as the forefront anode material for high-energy density lithium-ion batteries, owing to its exceptional specific capacity. Nevertheless, the traditional combination of polyacrylic acid binder and acetylene black conductive carbon continues to struggle with the immense stress induced by the repetitive volume expansion and contraction processes. Here we report a high ionic conductivity, sulfonyl fluoro-containing binder for SiO_x anode via free radical copolymerization reaction between perfluoro (4-methyl-3,6-dioxaoct-7-ene) sulfonyl fluoride and acrylic acid. The electrode fabrication process incorporated amino-functionalized carbon nanotubes (CNT-NH_2) as the conductive agent. A three-dimensional conductive network structure is constructed through physical and chemical double cross-linking interactions between the -COOH and -SO_2F functional groups of $PAF_{0.1}$ binder, the -NH_2 groups of CNT-NH_2, and the -OH groups on the surface of SiO_x, including hydrogen bonds and covalent bonds. In addition, the binder induces the formation of a solid electrolyte interphase (SEI) rich in inorganic components such as Li_2O, Li_2SO_3, Li_2CO_3, and LiF. Benefiting from the synergistic effects of the physically and chemically double cross-linked three-dimensional conductive network constructed by the $PAF_{0.1}$ binder and CNT-NH_2, coupled with the rich-inorganic SEI, the SiO_x anode delivers exceptional rate performance, cycle stability, and lithium-ion diffusion dynamics.

KEYWORDS
3D network structure, binder, physicochemical dual crosslinking, SiO_x

Gang Wu and Yuanhang Gao contributed equally to this work.

1 | INTRODUCTION

Amidst the intensifying urgency to resolve "low battery anxiety" in portable electronics, mitigate "range anxiety" in electric vehicles, and tackle "security anxiety" in large-scale energy storage systems, there exists a fervent anticipation for the emergence of lithium-ion batteries characterized by unparalleled energy density, exceptional rate performance, and formidable cycling sustainability.[1] However, as the representative of the forefront anode material for high-energy density lithium-ion batteries, silicon oxide (SiO_x) presents difficulties in meeting the urgent commercial demand due to various reasons.[2] Typically, the large volume expansion (~200%), low ionic electronic conductivity, and irreversible first discharge products (Li_2O and $Li_xSi_yO_z$) are three stumbling blocks for SiO_x to realize superior cycle stability, high rate performance, and enviable initial Coulombic efficiency (ICE).[3]

Generally, the binder, conductive agent and SiO_x are the main components of the electrode.[4] The interaction among different components is of vital importance to maintain the stability of the electrode structure.[5] Traditional polyacrylic acid (PAA) binders form irreversible covalent bonds with the polar groups of SiO_x, making them unable to withstand the large volume fluctuations during cycling.[6] This leads to particle fragmentation and continuous solid electrolyte interphase (SEI) rupture, resulting in poor cycle stability and notably low ICE. Furthermore, traditional acetylene black (CB) conductive agents lack polar groups on their surface, relying solely on weak van der Waals forces to maintain electrical contact between SiO_x and the current collector.[7] Consequently, when SiO_x particles undergo pulverization due to volume expansion during cycling, the electrical connectivity with the current collector and among SiO_x particles is compromised. The quest for suitable binders and conductive agents becomes imperative to establish robust electrical connections within the electrode structure.[8]

In this work, a high ionic conductivity, sulfonyl fluoro-containing binder, namely PAF binder, for SiO_x anode was synthesized via free radical copolymerization reaction between perfluoro (4-methyl-3,6-dioxaoct-7-ene) sulfonyl fluoride (PFSF) and acrylic acid (AA). The electrode fabrication process incorporated amino-functionalized carbon nanotubes (CNT-NH_2) as the conductive agent. A three-dimensional conductive network structure is constructed through physical and chemical double cross-linking interactions between the -COOH and -SO_2F functional groups of $PAF_{0.1}$ binder, the -NH_2 groups of CNT, and the -OH groups on the surface of SiO_x, including hydrogen bonds and covalent bonds. This intricate network structure effectively preserved electrical connectivity among the binder, conductive agent, SiO_x particles, and the copper current collector. Furthermore, the gradient hydrogen bonds in the three-dimensional network structure can gradually dissociate, effectively buffering the stress caused by the volume expansion of SiO_x. Additionally, compared to electrolyte components, the binder molecules exhibited a lower lowest unoccupied molecular orbital (LUMO) energy level. This characteristic made them more prone to preferential reduction on the anode surface during discharge, leading to the formation of a SEI composed of inorganic components like Li_2SO_3/Li_2CO_3 and LiF. Benefiting from the synergistic effects of the physically and chemically double cross-linked three-dimensional conductive network constructed by the $PAF_{0.1}$ binder and CNT-NH_2 conductive agent, coupled with the SEI rich in inorganic components, the SiO_x anode demonstrated exceptional rate performance, cycle stability, and lithium-ion diffusion dynamics.

2 | RESULTS AND DISCUSSION

2.1 | Theoretical calculation

To investigate the interactions between binders and CNT-NH_2, density functional theory (DFT) was employed to calculate the bond energies of various hydrogen bonds and covalent bonds. Previous research indicates that the -COOH groups in AA and the -NH_2 groups in CNT-NH_2 can undergo an amidation reaction during drying at 150°C, forming covalent amide bonds.[9] Moreover, hydrogen bonds are observed between the polar -COOH and -SO_2F groups of the PAF_x binder and the -NH_2 groups of the CNT-NH_2. In Figure 1c, there is an illustration of an S = O • • • H-OOC hydrogen bond with a bond energy measuring 2.39 kcal mol^{-1} between PFSF and AA molecules. Additionally, there is a depiction of a C = O • • • H-OOC hydrogen bond with a higher bond energy of 20.08 kcal mol^{-1} between AA molecules. Additionally, an S = O • • • H-NH hydrogen bond with a bond energy of 2.86 kcal mol^{-1} is observed between PFSF and CNT-NH_2. Furthermore, there are COO-H • • • H-NH hydrogen bonds (2.99 kcal mol^{-1}) and covalent amide bonds (C = O-NH) with a significantly higher bond energy (271.71 kcal mol^{-1}), linking AA and CNT-NH_2. The observations indicate that the resilient three-dimensional framework established by potent covalent bonds featuring high bond energy between AA and CNT-NH_2 plays a pivotal role in upholding the structural integrity of the SiO_x anode. Additionally, the gradient hydrogen bonds between AA, PFSF, and

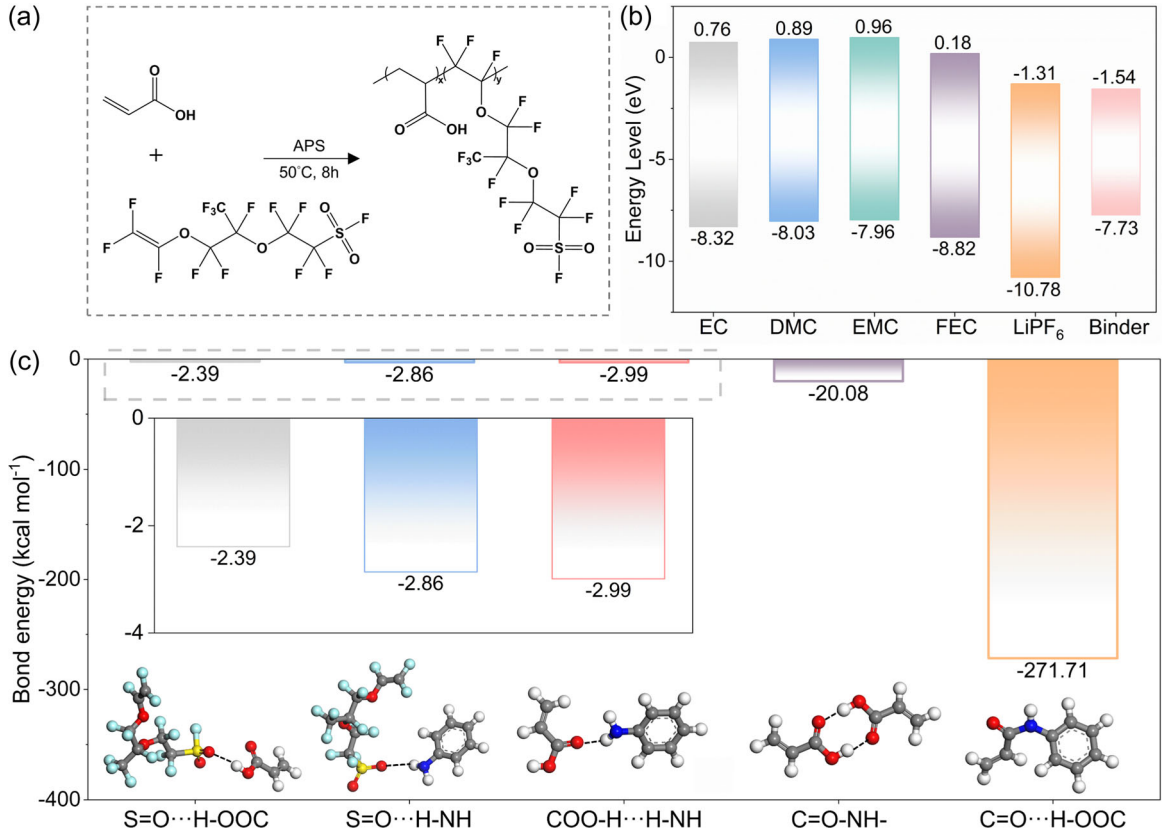

FIGURE 1 (a) AA and PFSF monomers are free radically polymerized to synthesize PAF binder. (b) Frontier molecular orbitals of different compounds. (c) The hydrogen bond types and bond energies calculated by density functional theory simulations. AA, acrylic acid; APS, ammonium persulfate; PFSF, perfluoro (4-methyl-3,6-dioxaoct-7-ene) sulfonyl fluoride.

$CNT\text{-}NH_2$ can be progressively dissociated, effectively mitigating the stress resulting from the volume expansion of SiO_x. This comprehensive understanding of bond energies and interactions aids in designing electrodes with enhanced stability and performance.

To explore in depth the influence of binders on SEI components, DFT was used to continue to evaluate the molecular orbital energy levels of various electrolytes and binders.[10] Figure 1b illustrates that binder molecules exhibit lower LUMO energy levels compared to electrolyte components like ethylene carbonate (EC), dimethyl carbonate, ethyl methyl carbonate, floroethylene carbonate (FEC), and $LiPF_6$. A lower LUMO energy level signifies a higher electron affinity, making it easier for the binder molecules to undergo reduction on the anode surface during the discharge process, leading to the formation of SEI components. Specifically, the binder molecule with the lowest LUMO energy level suggests that PFSF molecules enriched with $-SO_2F$ groups are more inclined to be preferentially reduced on the anode surface. Consequently, this results in the creation of an SEI that is rich in inorganic components. This insight into molecular orbital energy levels aids in understanding the electrochemical processes occurring at the electrode–electrolyte interface and underscores the role of binders in influencing SEI composition, which is crucial for optimizing battery performance and stability.

2.2 | Synthesis and characterization of PAF binder

To unveil the chemical structures of the PFSF, AA, and $PAF_{0.1}$, Fourier transform infrared spectroscopy (FTIR) analysis was employed. As depicted in Figure 2a, the spectrum of PFSF reveals a minor peak at 1839 cm^{-1}, indicative of the stretching vibration associated with its C = C double bond. Notably, two distinct peaks at ~1464 and 1234 cm^{-1} emerge, correlating respectively to the symmetric and asymmetric stretching vibrations of $-SO_2-$. A cluster of minor peaks around 1150 cm^{-1} is attributed to the stretching vibration of the carbon-fluorine (C-F) bond. Furthermore, a sharp peak at 984 cm^{-1} signifies the stretching vibration of the C-O-C bond. Noteworthy is the broad peak at 810 cm^{-1}, coupled with a sharp peak at 606 cm^{-1}, indicative of the presence of the S-F and C-S

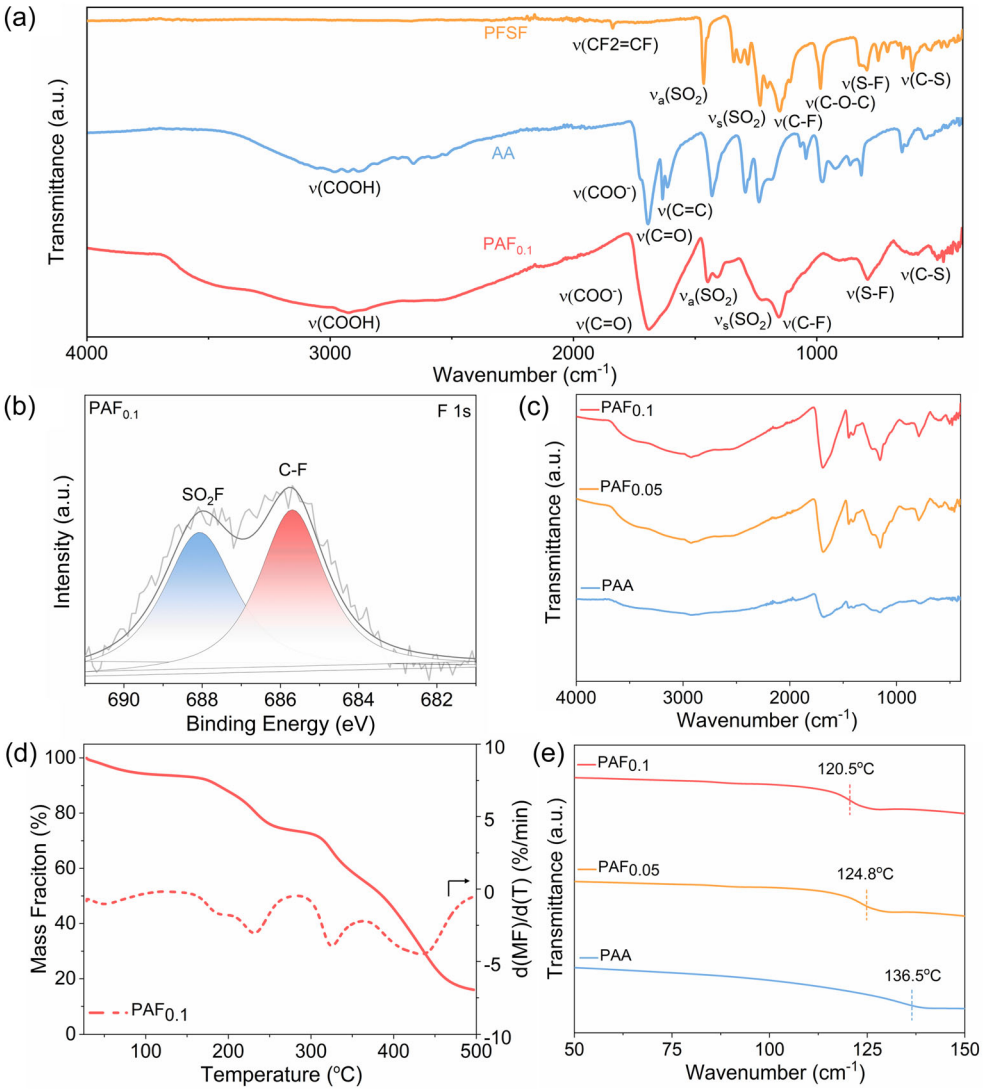

FIGURE 2 (a) FTIR spectra of PFSF, AA, and $PAF_{0.1}$. (b) The F 1*s* XPS spectrum of $PAF_{0.1}$. (c) FTIR spectra of $PAF_{0.1}$, $PAF_{0.05}$, and PAA. (d) The TGA and corresponding differential thermal analysis curves of $PAF_{0.1}$. (e) The DSC curve of $PAF_{0.1}$, $PAF_{0.05}$, and PAA. AA, acrylic acid; DSC, differential scanning calorimetry; FTIR, Fourier transform infrared spectroscopy; PAA, polyacrylic acid; PFSF, perfluoro (4-methyl-3,6-dioxaoct-7-ene) sulfonyl fluoride; TGA, thermogravimetric analysis; XPS, X-ray photoelectron spectroscopy.

bonds, respectively.[11] The spectrum of AA reveals a broad peak spanning from 2751 to 3331 cm^{-1}, indicative of the hydroxyl stretching vibration within the carboxyl group (-OH in -COOH).[12] Additionally, the small peak at 1724 cm^{-1} corresponds to the -COO- stretching vibration in the carboxyl group. The absorption peaks observed at 1693 and 1613 cm^{-1} are attributed to the stretching vibration of the C = O bond and C = C bond, respectively.[13] In the $PAF_{0.1}$ copolymer, the characteristic peaks associated with the C = C bonds disappear around 1839 and 1613 cm^{-1}, whereas new peaks from the sulfonyl fluoride group (-SO_2F) of PFSF and the carboxyl group (-COOH) of AA emerge. Compared with PFSF monomer, C-F in $PAF_{0.1}$ undergoes a blue shift due to the steric hindrance effect between functional groups after copolymerization. This provides evidence of copolymerization events taking place. Figure 2b depicts the utilization of X-ray photoelectron spectroscopy (XPS) analysis to investigate the groups present in $PAF_{0.1}$. The F 1*s* spectrum clearly exhibits two peaks, located at ~688.1 and 685.7 eV, corresponding to SO_2F and C-F, respectively, indicating the presence of PFSF in the copolymer $PAF_{0.1}$.

Given the above results, FTIR was carried out to detect the prevalence of hydrogen bonding in PAF_x ($x = 0.05$ or 0.1). As illustrated in Figure 2c, the distinctive peak at approximately 1689 cm^{-1} in the PAA spectrum corresponds to the stretching vibration of C = O. Conversely, in the spectrum of $PAF_{0.05}$ and $PAF_{0.1}$, the C = O stretching vibration peaks red shift to

1686 and 1684 cm^{-1}, respectively. The slight red shift of C = O proves the participation of C = O in the formation of hydrogen bonds. Additionally, the magnitude of red shift and intensity of the characteristic peak increase with the proportion of PFSF. Furthermore, the stretching vibration peak of -OH in COOH displays a broadening effect. The asymmetric and symmetric stretching vibrations of -SO_2- in the sulfonyl fluoride group exhibit a red shift in PAF_x, occurring at 1449 and 1227 cm^{-1}, respectively. Moreover, the stretching vibration peak of the S-F bond in the sulfonyl fluoride group (located at 791 cm^{-1}) also exhibits a red shift phenomenon. In conclusion, the observed red shift and broadening phenomena of the characteristic peaks in PAF_x are indicative of the presence of hydrogen bonding interactions between the sulfonyl fluoride group (-SO_2F) in PFSF and the carboxyl group (-COOH) in AA.

Thermal stability assessment of $PAF_{0.1}$ was conducted using thermogravimetric analysis (TGA). As depicted in Figure 2d, $PAF_{0.1}$ exhibits characteristic degradation behavior across multiple stages. Beyond 160°C, the copolymer undergoes a minor degradation attributed to water loss. Upon surpassing 160°C, the copolymer initiates its first degradation stage, whereas the anhydration reaction involving carboxyl groups persists until temperatures exceed 283°C.[12] The third stage of decomposition ranges from 300°C to 363°C, mainly from the decomposition of acrylic anhydride. The subsequent degradation stage between 365°C and 460°C arises from the decomposition of the sulfonyl fluoride group.[14] With further temperature escalation, $PAF_{0.1}$ copolymer begins to carbonize.[15] Notably, the TGA curve illustrates the copolymer's retention of thermal stability across a broad temperature range below 160°C, a feature advantageous for alleviating safety concerns in lithium-ion batteries.

The glass transition temperature (T_g) of the polymers was investigated using differential scanning calorimetry. As depicted in Figure 2e, PAA exhibits a higher T_g value of 136.5°C compared to $PAF_{0.05}$ and $PAF_{0.1}$, with T_g values of 124.8°C and 120.5°C, respectively. This phenomenon arises due to the exclusive presence of C = O • • • H-OOC hydrogen bonds between AA molecules within the PAA binder, exhibiting a remarkably high bond energy of 20.08 kcal mol^{-1}. However, upon the introduction of PFSF molecules into the polymer binder, S = O • • • H-OOC hydrogen bonds with a bond energy of only 2.39 kcal mol^{-1} are generated between PFSF and AA molecules. In $PAF_{0.05}$ and $PAF_{0.1}$ binders, because some AA molecules participate in the formation of S = O • • • H-OOC hydrogen bonds, the proportion of C = O • • • H-OOC hydrogen bonds between AA and AA molecules decreases. Substitution of the high bond energy C = O • • • H-OOC hydrogen bond with the lower bond energy S = O • • • H-OOC hydrogen bond leads to a reduction in the intermolecular force within the PAF_x structure. Notably, as the proportion of PFSF monomers increases, there is a corresponding increase in the replacement of C = O • • • H-OOC hydrogen bonds with S = O • • • H-OOC hydrogen bonds, further weakening the intermolecular forces within PAF_x. Consequently, the T_g experiences a gradual decline in PAA, $PAF_{0.05}$, and $PAF_{0.1}$ binders due to these structural modifications.

In the spectra of pure $PAF_{0.1}$ and $PAF_{0.1}$ combined with SiO_x as a binder (Supporting Information S1: Figure S3), noticeable differences are observed. Specifically, compared to the pure $PAF_{0.1}$ binder, a distinct -COO- peak is observed at 1722 cm^{-1} in the combined spectrum. This observation serves as evidence of an esterification reaction occurring between the -COOH functional group of the $PAF_{0.1}$ binder and the -OH groups of SiO_x. Additionally, several spectral changes are noted: the stretching vibration of -OH in -COOH, the symmetrical absorption peak of -SO_2, and the stretching vibration peak of the S-F bond all exhibit broader profiles. These broadening effects are indicative of the presence of hydrogen bonds between the -SO_2F and -COOH functional groups of the binder and the -OH groups of SiO_x.

Supporting Information S1: Figure S4 shows the scanning electron microscopy (SEM) image and energy spectrum of the CNT-NH_2. As shown in the figure, the diameter of the carbon nanotube is about 50 nm and the length is several microns. The energy spectrum results show that the nitrogen element on the surface of the carbon nanotube is evenly distributed in a point-like manner, indicating that -NH_2 is evenly distributed on the surface of the carbon nanotube. To explore the interaction between the polymer binder and the CNT-NH_2 conductive agent, XPS tests were performed on their mixtures. For instance, the N 1*s* spectrum (Supporting Information S1: Figure S5) reveals distinct characteristics: solely the C-N peak at 399.2 eV is discerned for pure CNT-NH_2. However, upon the addition of PAA or PAF_x, a prominent O = C-N covalent bond peak emerges at 398.5 eV, as depicted in Figure 3a–c. Moreover, the introduction of PFSF monomer causes the area of the covalent O = C-N peak to gradually increase. This increase signifies a rising degree of amidation between the polymer binder and the CNT-NH_2 conductive agent, indicating that PFSF can promote the amidation reaction between AA and CNT-NH_2. This effect may stem from the highly electronegative perfluorinated side chain present in the PFSF monomer, which exerts a strong electron-withdrawing influence. This renders the -COOH group in the AA monomer more acidic, thus facilitating

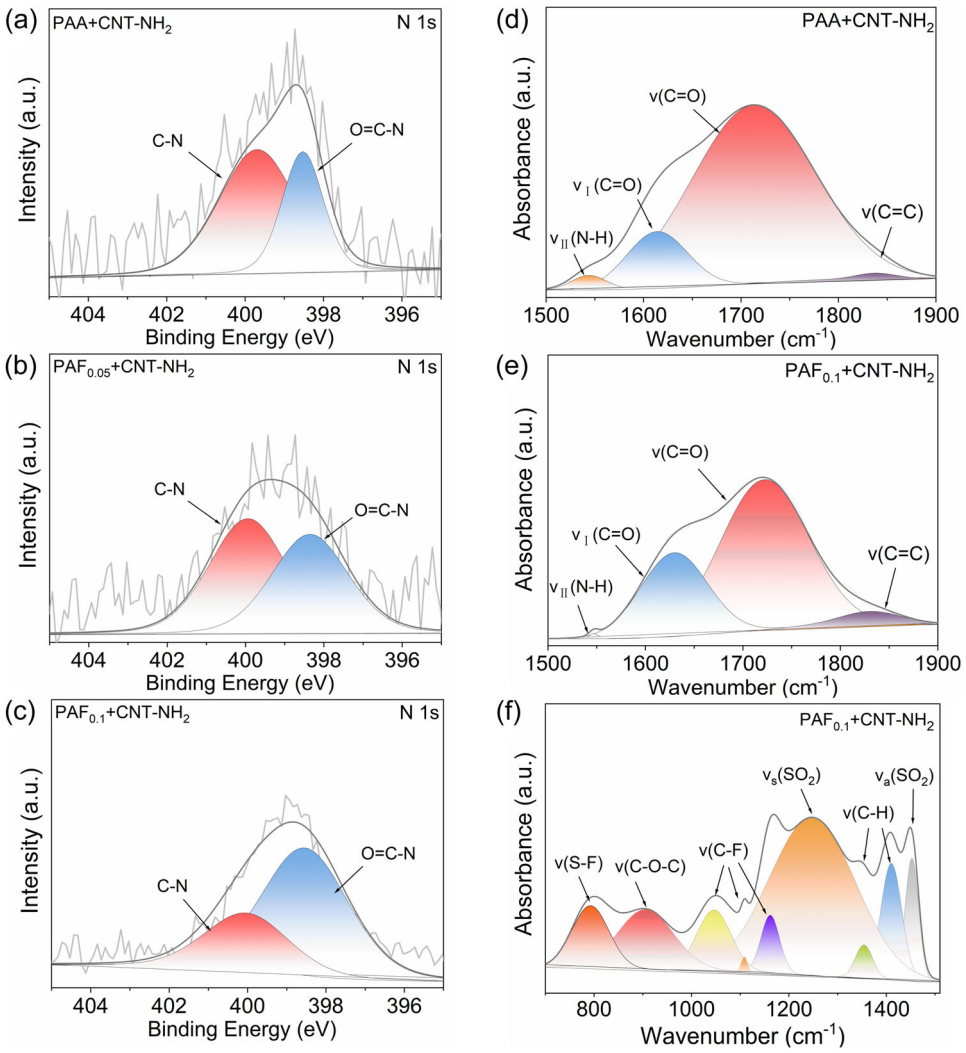

FIGURE 3 The comparison of XPS N 1*s* spectra of (a) PAA-CNT-NH_2, (b) $PAF_{0.05}$-CNT-NH_2, (c) $PFA_{0.1}$-CNT-NH_2. FTIR spectra of (d) PAA-CNT-NH_2, (e) $PAF_{0.05}$-CNT-NH_2, (f) $PFA_{0.1}$-CNT-NH_2. CNT-NH_2, amino-functionalized carbon nanotube; FTIR, Fourier transform infrared spectroscopy; PAA, polyacrylic acid; XPS, X-ray photoelectron spectroscopy.

its reactivity in undergoing an amidation reaction with the -NH_2 groups of carbon nanotubes. Furthermore, this phenomenon is also evident in the C 1 s spectrum of their mixture (Supporting Information S1: Figure S6).[16]

To delve further into the interaction between the $PAF_{0.1}$ binder and the CNT-NH_2 conductive agent, FTIR tests were conducted on their mixtures. The results, as depicted in Figure 3d, reveal distinct peaks in the range of 1500–1900 cm^{-1}, attributed to various components such as C = C, COOH, C = O, and N-H functionalities.[17] These peaks correspond to the carbon skeleton of CNT-NH_2, the carboxyl group of the AA monomer, the amide I band (C = O), and the amide II band (N-H), respectively. Upon comparison with the spectrum of pure $PAF_{0.1}$ (Figure 3e), noticeable changes are observed. Specifically, a red shift in the -COOH peak indicates the formation of a hydrogen bond between the -COOH group of the $PAF_{0.1}$ binder and the -NH_2 group of the CNT-NH_2 conductive agent. Additionally, the appearance of the amide I band (C = O) and the amide II band (N-H) further confirms the occurrence of an amidation reaction between the -COOH group of the $PAF_{0.1}$ binder and the -NH_2 group of the CNT-NH_2 conductive agent.[18] As depicted in Figure 3f, distinct peaks corresponding to the asymmetric stretching vibration of -SO_2- and the stretching vibration of S-F are observed at 1441 and 790 cm^{-1}, respectively, within the range of 700–1500 cm^{-1}. Compared with the spectrum of pure $PAF_{0.1}$, the red shift of the -SO_2- peak and the S-F peak indicates the formation of hydrogen bonds between the -SO_2- group of the $PAF_{0.1}$ binder and the -NH_2 group of the CNT-NH_2.

2.3 | Mechanical properties

Figure 4a depicts the load-displacement curves obtained from nano-indentation tests on two polymer films, along with their respective hardness and elastic modulus values.[19] The PAA film demonstrates calculated values of 381.1 MPa for hardness and 9.34 GPa for elastic modulus, as depicted in Figure 4b. In contrast, $PAF_{0.1}$ shows lower hardness (316.6 MPa) and elastic modulus (8.67 GPa). The diminished elastic modulus and hardness observed in $PAF_{0.1}$ can be attributed to the introduction of flexible PFSF monomer, which makes C = O • • • H-OOC with high bond energy (20.08 kcal mol^{-1}) being replaced by S = O • • • H-OOC with low bond energy (2.39 kcal mol^{-1}), reducing the intermolecular force. The low Young's modulus indicates that the $PAF_{0.1}$ binder has better deformation ability. When SiO_x volume expands, it can effectively dissipate internal stress through the gradient dissociation and reconstruction of hydrogen bonds between -COOH and $-SO_2F$ functional groups.

The inclusion of PFSF is expected to have a substantial impact on the rheological properties of PAF0.1 polymer molecules, a phenomenon that can be confirmed through rheometer analysis (Figure 4c). At the same concentration, both storage modulus (G') and loss modulus (G") of the $PAF_{0.1}$ solution are higher than those of the PAA solution, indicating that the $PAF_{0.1}$ solution has enhanced elastic deformation recovery and viscous deformation dissipation capabilities.[19a] This may be attributed to the gradient dissociation and reconstruction of hydrogen bonds between functional groups under shear stress. The complex viscosity of the two polymer solutions was measured at a concentration

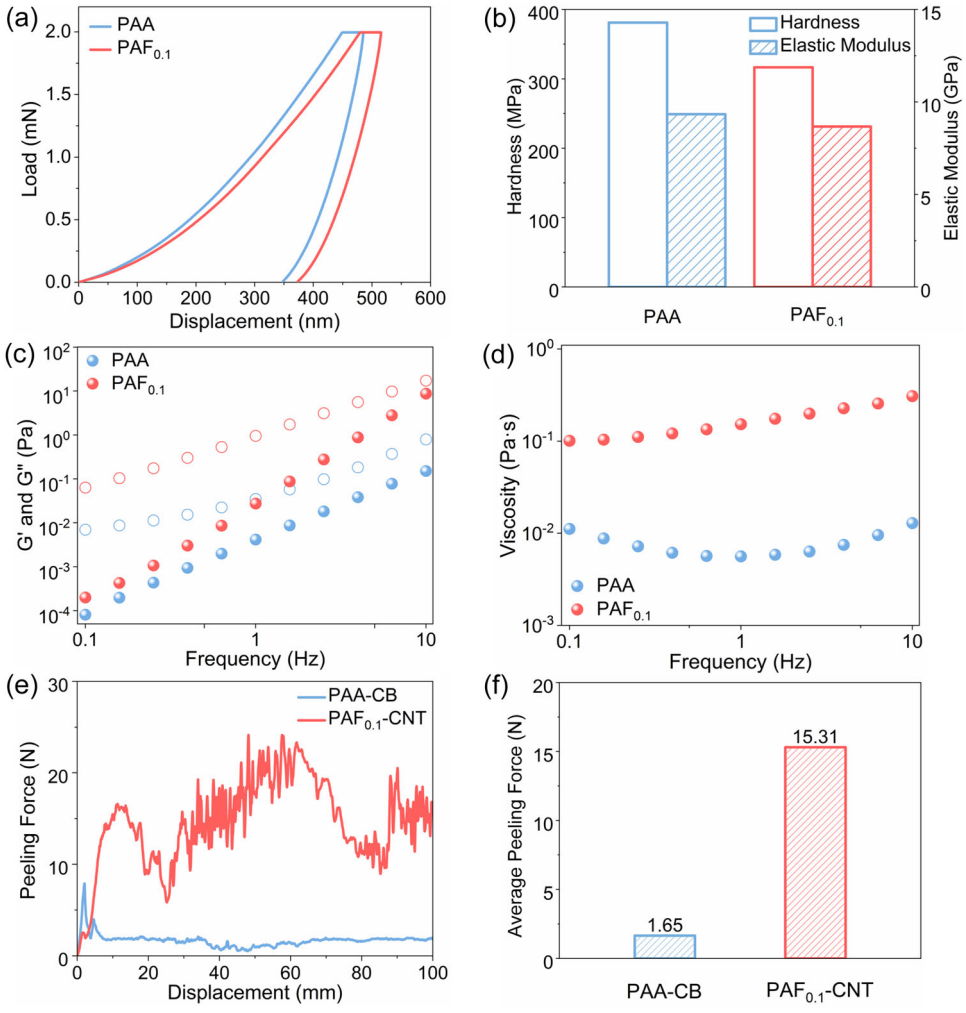

FIGURE 4 (a) The load-displacement curves of PAA and $PAF_{0.1}$ films in nano-indentation test and (b) corresponding hardness and elastic modulus. (c) The rheological properties of 5 wt% PAA and $PAF_{0.1}$ aqueous solution. (d) Complex viscosities of 5 wt% PAA and $PAF_{0.1}$ aqueous solution. (e, f) 180° peeling curves and average peeling force of SiO_x electrodes with PAA-CB and $PAF_{0.1}$-CNT. CB, acetylene black; CNT, carbon nanotube; PAA, polyacrylic acid.

of 5 wt% (Figure 4d). The complex viscosity of $PAF_{0.1}$ is higher from low frequency (0.1 Hz, 0.1009 Pa s) to high frequency (10 Hz, 0.3080 Pa s), whereas the values for PAA are lower than 0.0111 Pa s (0.1 Hz) and 0.0129 Pa s (10 Hz).

In general, the viscosity of $PAF_{0.1}$ is ~23 times greater than that of PAA, suggesting that $PAF_{0.1}$ experiences significantly higher internal friction. Mainly due to the longer perfluorinated side chains of $PAF_{0.1}$, it is more likely to become entangled when subjected to shear stress, resulting in an increase in viscosity. The adhesion capability of binders plays a critical role in preventing active material detachment and maintaining electrode integrity. To assess their adhesion ability, typical 180° peel tests were conducted on SiO_x electrodes using different binders. As depicted in Figure 4e,f, the $PAF_{0.1}$-CNT electrode (15.31 N) consistently exhibited higher peel force throughout the entire peel-off process, nearly nine times that of the PAA-CB electrode (1.65 N). This result underscores the superior adhesion capability of the $PAF_{0.1}$ binder over PAA binder. Remarkably, this excellent performance is achieved with only 10% content of the binder $PAF_{0.1}$, which is significantly less than the 20% content of PAA-CB. The primary reason for the difference in performance between the PAA-CB and $PAF_{0.1}$-CNT anodes lies in the choice of conductive agent. The PAA-CB anode utilizes traditional CB, which lacks polar groups on its surface and can only establish a connection with the binder through weak van der Waals forces. In contrast, the $PAF_{0.1}$-CNT anode employs an amino-functionalized CNT-NH_2 conductive agent, characterized by numerous -NH_2 on its surface. These -NH_2 enable the conductive agent to form connections with the binder through gradient hydrogen bonds and covalent amide bonds, resulting in the formation of a robust three-dimensional network structure. This fully proves that the three-dimensional network structure mediated by physical and chemical double cross-linking has unique advantages in improving the electrode connection strength and maintaining the integrity of the electrode structure.

2.4 | Electrochemical performances of different electrodes

To investigate the reduction stability of the adhesive, linear sweep voltammetry testing was initially conducted on the binder film coated on copper foil. The results, as depicted in Supporting Information S1: Figure S7, show three distinct reduction peaks at 1.73, 1.47, and 0.78 V, respectively, as the potential sweeps from 3 to 0 V. These peaks correspond to the reduction and decomposition processes of the binder, FEC, and EC, respectively.[20] The observation that the binder decomposes preferentially over the electrolyte aligns with the theoretical calculation results. Compared to the inorganic components such as carboxylates generated from the decomposition of solvents like EC and FEC, the binder's decomposition, rich in -SO_2F groups, leads to the formation of inorganic components such as Li_2O, Li_2SO_3, and LiF. These inorganic components contribute to a higher mechanical strength of the SEI, aiding in maintaining the structural integrity of silicon oxide particles.

The electrochemical performance of SiO_x-based electrodes using various binders and conductive agents was systematically evaluated through a series of half-cell tests. To verify the uniform electrochemical behavior of SiO_x particles, a cyclic voltammetry (CV) test was conducted using PAF as the binder, and the results are illustrated in Figure 5a. In the initial cycle, two distinct reduction peaks are evident at 1.89 V and 1.39 V in the $PAF_{0.1}$-CNT anode. These peaks correspond to the reduction and decomposition processes of the $PAF_{0.1}$ binder and the electrolyte on the SiO_x surface, respectively.[21] This observation aligns well with the theoretical calculation results. Furthermore, a conspicuous reduction peak is observed at 0.15 V, indicative of the formation of a Li-Si alloy. Moreover, broader peaks around 0.34 V and 0.53 V were identified as the delithiation stages of the Li-Si alloy. During the subsequent scan cycles, it was noted that the reduction peak at 1.39 V disappeared. However, the reduction peak at 1.89 V persisted and shifted slightly to 1.83 V. This shift indicates that the continuous reduction and decomposition of the binder led to the formation of a stable structure on the SiO_x surface, known as the SEI. This stable SEI structure serves to prevent the continuous decomposition of the electrolyte, contributing to improved stability and performance of the anode. Moreover, the intensity of three main redox peaks mentioned above progressively increased with cycling, indicating the infiltration of electrolyte into the electrode and the electrochemical activation of SiO_x. These findings provide valuable insights into the electrochemical behavior and activation mechanisms of SiO_x-based electrodes, highlighting the role of PAF as a binder in facilitating stable electrochemical processes.

The initial charge-discharge curve of the SiO_x anode with PAA-CB, PAA-CNT, $PAF_{0.05}$-CNT, or $PAF_{0.1}$-CNT at a rate of 0.1 C is shown in Figure 5b. Notably, an important observation is that the ICE of the PAF system anode (72.66% and 74.11%) exceeds that of the PAA system anode (70.47% and 70.55%). Furthermore, it's noted that the higher the PFSF content is, the higher the

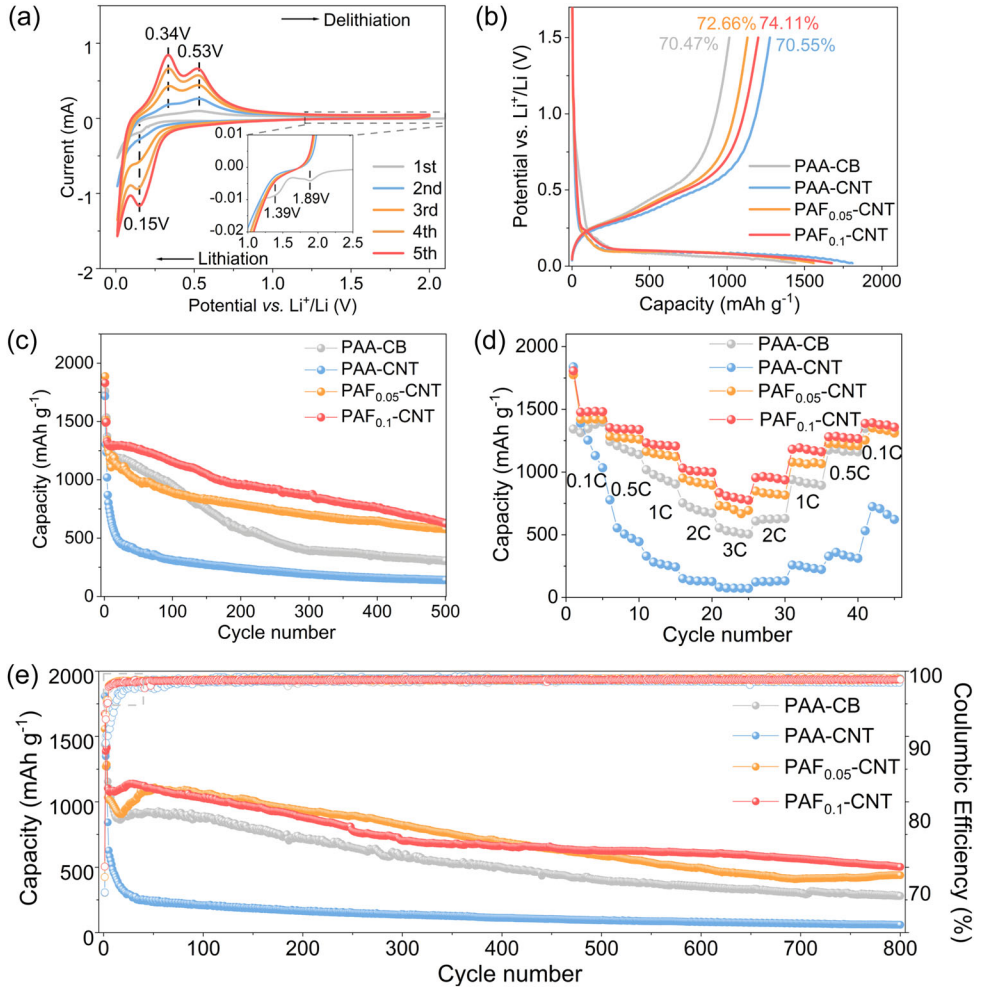

FIGURE 5 (a) CV profiles of SiO_x@$PAF_{0.1}$-CNT anode. (b) Galvanostatic charge–discharge profiles of different anodes at the first cycle. (c) Cycling performances of different anodes at 0.5 C. (d) Rate performances of different anodes. (e) Cycling performances of different anodes at 1 C. CB, acetylene black; CNT, carbon nanotube; CV, cyclic voltammetry; PAA, polyacrylic acid.

ICW will be. On the one hand, this is due to the increase in PFSF monomer and the gradual increase in the degree of amidation reaction between the binder and carbon nanotubes, forming a tighter three-dimensional conductive network, which can provide efficient conductive pathways and maintain a more complete electrode structure. On the other hand, it may be that the $PAF_{0.1}$ binder has a lower LUMO energy level and decomposes preferentially than the electrolyte, promoting the formation of a stable SEI.

Figure 5c illustrates the constant current cycling performance of SiO_x anodes utilizing PAA-CB, PAA-CNT, $PAF_{0.05}$-CNT, or $PAF_{0.1}$-CNT at a rate of 0.5 C. The initial discharge capacities for PAA-CB, PAA-CNT, $PAF_{0.05}$-CNT, and $PAF_{0.1}$-CNT anodes are recorded as 1760.8, 1718.4, 1888.2, and 1830.5 mAh g^{-1}, respectively. Throughout subsequent cycles, PAA-CB and PAA-CNT anodes exhibit rapid capacity decay, with PAA-CNT demonstrating a faster decline. In contrast, the capacity decay of $PAF_{0.05}$-CNT and $PAF_{0.1}$-CNT anodes is relatively slower. In the first 250 cycles, the capacity of the PAA-CB anode dropped rapidly to below 500 mAh g^{-1} (capacity retention rate 27.1%), and it remained basically stable until 300 cycles. After 500 cycles, it only maintained a capacity of 308.8 mAh g^{-1} (capacity retention rate 17.5%) and the average Coulombic efficiency only 99.66%. The rapid capacity loss observed in the PAA-CB anode can be attributed to the partial breakage of covalent bonds between hydroxyl and carboxyl groups following the volume expansion of SiO_x. Moreover, there is only a weak van der Waals force between the CB conductive agent, PAA binder, and SiO_x particles, which cannot form an effective conductive path. The capacity of the PAA-CNT anode experienced a rapid decline, dropping below 500 mAh g^{-1} (capacity retention rate 28.3%) after only 20 cycles. Eventually, it stabilized at a capacity of 141.8 mAh g^{-1} (capacity retention rate 8.2%) after 500 cycles, with an average Coulombic efficiency as

low as 99.54%. This decline can be attributed to several factors. First, the low binder content in the PAA-CNT negative electrode hinders its ability to effectively connect with SiO_x particles. This lack of connectivity results in reduced capacity and performance over cycles. Additionally, the presence of only strong covalent bonds between the binder and the carbon nanotube conductive agent is insufficient to withstand the volume expansion of SiO_x. Without an effective mechanism to buffer stress during expansion, the covalent bonds eventually break, further contributing to the decline in capacity and efficiency of the anode. Conversely, the incorporation of sulfonyl fluoride groups mitigated this issue by enhancing hydrogen bonds with carboxyl and amino groups. As a result, the reversible capacity of the $PAF_{0.05}$-CNT anode improved significantly to 580.1 mAh g^{-1} (capacity retention rate 30.7%), with an average Coulombic efficiency of 99.74% after 500 cycles. Moreover, as the content of sulfonyl fluoride groups increased, the reversible capacity also increased. Notably, the $PAF_{0.1}$-CNT anode exhibited the highest reversible capacity of 627.3 mAh g^{-1} (capacity retention rate 34.3%), with an average Coulombic efficiency value of 99.76%. The above results fully prove that at lower binder and conductive agent contents, the introduction of PFSF monomer can enable the binder to form a covalent–noncovalent three-dimensional conductive network through gradient hydrogen bonds and covalent amide bonds, which is effective Buffers SiO_x volume expansion and improves cycle stability.

Figure 5d illustrates the rate performance of various anodes. The $PAF_{0.1}$-CNT anode demonstrates capacities of 1477.4, 1343.3, 1214.6, 1003.2, and 797.6 mAh g^{-1} at rates of 0.1, 0.5, 1, 2, and 3 C, respectively. Additionally, upon reverting the cycling rate to 0.1 C, the $PAF_{0.1}$-CNT anode maintains a substantial capacity of 1392.8 mAh g^{-1}. In contrast, the PAA-CNT anode exhibited capacities of 282.5, 135.8, and 82.4 mAh g^{-1} at rates of 1, 2, and 5 C, respectively. Upon returning to 0.1 C, it retained a capacity of 708.4 mAh g^{-1}, showing a rapid decreasing trend. The huge contrast in rate performance between PAA-CNT anode and $PAF_{0.1}$-CNT anode under high current density fully proves that the huge volume expansion of SiO_x cannot be fully accommodated through the irreversible covalent three-dimensional network alone. The stable SEI and covalent-noncovalent synergy formed after the introduction of PFSF monomer can better maintain the three-dimensional conductive network structure and improve the rate performance of SiO_x.

To further verify the long-term cycle stability of different binders, a constant current cycle at a rate of 1 C was performed in Figure 5e. All cells were first cycled at 0.1 C for three cycles to activate and subsequently at 1 C. After activation, the reversible discharge capacities of SiO_x electrodes with PAA-CB, PAA-CNT, $PAF_{0.05}$-CNT, and $PAF_{0.1}$-CNT were 1156.6, 843.5, 1034.8, and 1104.5 mAh g^{-1}, respectively. After 800 cycles, the $PAF_{0.1}$-CNT anode showed a reversible capacity of 502.9 mAh g^{-1}, which was much higher than PAA-CB (280.7 mAh g^{-1}) and PAA-CNT (60.7 mAh g^{-1}). The $PAF_{0.1}$-CNT anode showed an excellent capacity retention of 84.9% over the first 300 cycles, retaining 45.5% of the capacity after 800 cycles relative to activation. In contrast, the PAA-CB anode only had a capacity retention of 24.3% after 800 cycles. What's more, the PAA-CNT anode experienced severe capacity loss in the first 30 cycles, maintaining a capacity of 280.1 mAh g^{-1} at the 30th cycle and a low capacity retention rate of 7.2% after 800 cycles. To improve the performance of the SiO_x anode, we assembled a complete battery by pairing different anodes with $LiNi_{0.6}Co_{0.2}Mn_{0.2}O_2$ (NCM) cathodes. Supporting Information S1: Figure S8 shows that at 0.5 C, the $PAF_{0.1}$-CNT|NCM full cell exhibits significantly more reversibility and lower capacity attenuation (0.38%/cycle) than PAA-CB | NCM over 50 cycles, and more stable cycle performance (1C = 200 mAh g^{-1}). This result proves that the physicochemical dual crosslinking conductive network of PAF_x-CNT can effectively buffer enormous volume changes of SiO_x by the gradient hydrogen bond and covalent bond among -COOH, $-SO_2F$, and $-NH_2$.

High-resolution XPS analysis was employed to examine the interfacial stability of the SEI on the SiO_x electrode surface following 50 cycles. Within the C 1*s* spectrum, discernible peaks corresponding to C − H/C − C, C − O, C = O, and Li_2CO_3/$ROCO_2Li$ are identified in the PAA-CB electrode at 284.8, 286.1, 287.1, and 290.2 eV, respectively (Figure 6a,b). These organic constituents within the SEI are indicative of electrolyte decomposition. Conversely, a reduction in peak intensity for each C peak was observed in the $PAF_{0.1}$-CNT electrode, suggesting that the surface-stable SEI effectively mitigates electrolyte decomposition. In the O 1*s* spectrum (Figure 6c,d), heightened intensities of peaks at 531.7 eV (Li_2CO_3) and 529.7 eV (Li_2O) are observed on the $PAF_{0.1}$-CNT electrode. It is worth noting that the peak of Li_2CO_3 is shifted relative to the corresponding peak in PAA-CB, which may be due to the introduction of Li_2SO_3 into the SEI by the modified additives. In the F 1*s* spectrum (Figure 6e,f), two distinct peaks emerged: $Li_xPO_yF_z$ (687.2 eV) and LiF (684.6 eV), indicative of FEC and $LiPF_6$ decomposition. However, in the F 1*s* XPS spectrum of the $PAF_{0.1}$-CNT anode, the LiF peak intensity is higher, which is beneficial to improving the stability of SEI, and an obvious RSO_2F peak appears at

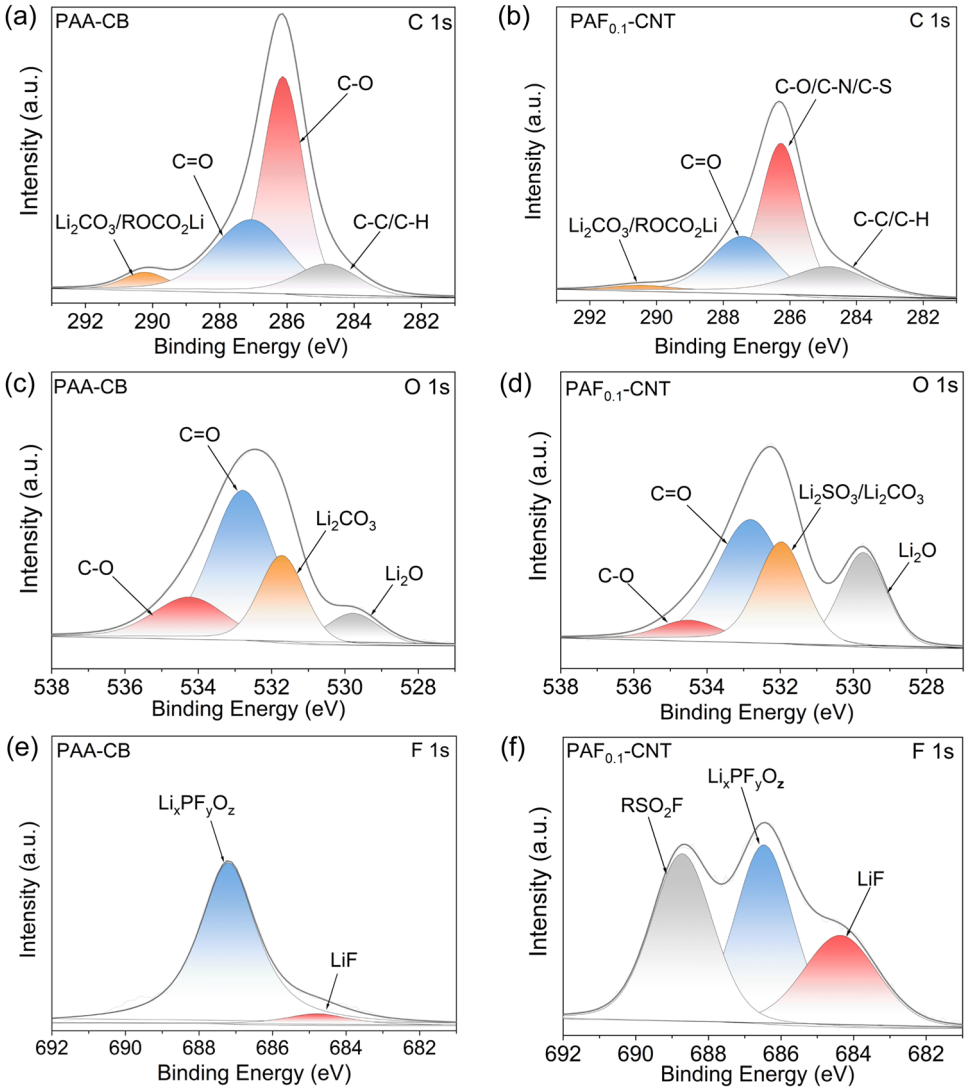

FIGURE 6 (a, b) C 1*s*, (c, d) O 1*s*, and (e, f) F 1*s* XPS spectra of various anodes after 50 cycles. CB, acetylene black; CNT, carbon nanotube; PAA, polyacrylic acid; XPS, X-ray photoelectron spectroscopy.

688.7 eV, which originates from incomplete decomposition of sulfonyl fluoride binder. As shown in Supporting Information S1: Figure S9, compared with PAA-CB, the LiF content on the surface of $PAF_{0.1}$-CNT anode increased by 4.5 times, while the Li_2O content increased by 1.6 times, and the Li_2SO_3/Li_2CO_3 content only increased by 10%. In the C 1*s* spectrum, compared with PAA-CB, the peak intensity of $Li_2CO_3/ROCO_2Li$ on the surface of $PAF_{0.1}$-CNT anode is lower, indicating that the content of Li_2CO_3 on the surface of $PAF_{0.1}$-CNT anode is lower. Therefore, the increase in Li_2SO_3/Li_2CO_3 content mainly comes from Li_2SO_3 produced by the decomposition of $-SO_2F$ group. The generation of Li_2SO_3 with high ion conductivity makes it easier for lithium ions to pass through the SEI and participate in the lithium deintercalation reaction of SiO_x, which is beneficial to reducing the R_{SEI} and R_{ct} of the $PAF_{0.1}$-CNT negative electrode. The above results fully prove that the $-SO_2F$ group in the $PAF_{0.1}$ binder with lower LUMO preferentially participates in the formation of SEI, promoting the generation of more nonpolar components such as Li_2O, Li_2SO_3/Li_2CO_3 and LiF.

To fully understand the composition and structure of SEI, the electrodes of different systems were characterized by XPS sputtering after 50 cycles. As shown in Supporting Information S1: Figure S10, with the extension of sputtering time, the content of LiF gradually increased, but the content of Li_2CO_3 and Li_2O did not increase significantly, and the content of C-O and other organic components gradually increased. Even if the sputtering time reached 120 s, some $Li_xPF_yO_z$ still existed. This indicates that the PAA-CB system cannot inhibit the penetration of the electrolyte into the electrode, which leads to the decomposition of the

infiltrated electrolyte into the inorganic components such as $Li_xPF_yO_z$ and $ROCO_2Li$ in the electrode. This kind of organic-inorganic co-existing SEI has low mechanical strength, which is not conducive to maintaining the stability of electrode structure. In contrast (Supporting Information S1: Figure S11), with the extension of sputtering time in $PAF_{0.1}$-CNT system, the contents of inorganic components such as LiF, Li_2CO_3/Li_2SO_3, and Li_2O gradually increased, while the contents of organic components such as $Li_xPF_yO_z$ and C-O gradually decreased. When the sputtering time reached 120 s, the contents of inorganic components such as $Li_xPF_yO_z$ and C-O gradually decreased. The $Li_xPF_yO_z$ signal is almost completely gone, only the LiF signal. The results show that the $PAF_{0.1}$-CNT system can effectively inhibit the electrolyte from penetrating into the electrode and avoid its decomposition into inorganic components such as $Li_xPF_yO_z$ and $ROCO_2Li$. In addition, the preferential decomposition of the binder in the electrode also promotes the formation of more inorganic components such as Li_2CO_3/Li_2SO_3 and Li_2O. This kind of internally rich inorganic SEI has high mechanical strength and is conducive to maintaining the stability of the electrode structure.

2.5 | Elastic properties of different electrodes

As previously mentioned, the PAF_x-CNT double cross-linked binder plays a pivotal role in stabilizing the electrode structure and mitigating volume changes. To delve deeper into the impact of physical and chemical double cross-linking on the macroscopic and electrode surface state postcycling, SEM was employed to compare surface morphology pre and post cycling. Figure 7 illustrates that the surfaces of both the PAA-CB and PAA-CNT anodes appeared rougher precycling compared to other variants. After 50 cycles, extensive cracks were observed on the PAA-CB and PAA-CNT anodes, especially the latter. This phenomenon may arise from poor compatibility between PAA fragments and SiO_x particles. Moreover, the micron-sized SiO_x particles in PAA-CNT are coated with a covalent network, resulting in an uneven surface prone to covalent bond breakage due to insufficient elasticity. In contrast, micrometer-sized pores visible precycling on the electrodes vanished on the PAF_x-CNT anode post-cycling. The healing of cracks on PAF_x-CNT anodes can be attributed to their introduction of more elastic noncovalent networks. The excellent elastic properties of this binder contribute to better cycling performance of PAF_x-CNT anodes. Further SEM analysis of cross-sectional morphology revealed that pre-cycling, the pristine PAA-CB and PAA-CNT anodes had thicknesses of 21.06 and 22.12 μm, respectively. Postcycling, their thicknesses significantly increased to 33.65 and 36.06 μm, respectively, with expansion rates of 59.8% and 63.0% (Figure 7m,n). In contrast, the $PAF_{0.05}$-CNT and $PAF_{0.1}$-CNT anodes only showed modest increases to 32.21 and 31.25 μm, with thickness increase rates of 48.9% and 39.8%, respectively (Figure 7o,p). Compared with the PAA-CB anode, the PAA-CNT anode has more and deeper surface cracks and a higher expansion rate, indicating that the covalent three-dimensional conductive network structure alone cannot suppress volume expansion and maintain the integrity of the electrode structure. The surfaces of $PAF_{0.05}$-CNT and $PAF_{0.1}$-CNT negative electrodes are smoother and have lower expansion rates. Mainly because after the introduction of PFSF monomer, the flexibility of the polymer binder increases. And the results show that the physicochemical double cross-linking mediated covalent and noncovalent three-dimensional network can maintain the integrity of electrode structure and promote the formation of stable SEI.

To explore the relationship between the excellent electrochemical performance of the $PAF_{0.1}$-CNT anode and its ionic conductivity, the Li^+ diffusion coefficient (D_{Li}^+) of SiO_x anode was meticulously examined using CV at varying scan rates. Supporting Information S1: Figure S12 showcases CV curves for the PAA-CB, PAA-CNT, $PAF_{0.05}$-CNT, and $PAF_{0.01}$-CNT anodes across scan rates ranging from 0.2 to 1.2 mV s^{-1}. The PAA-CNT anode exhibits an approximately fourfold increase in peak current intensity compared to the PAA-CB anode, demonstrating a substantial enhancement in electronic conductivity facilitated by the three-dimensional conductive network established by the CNT-NH_2 conductive agent within the electrode structure. Furthermore, the introduction of the PFSF monomer leads to a progressive increase in peak current intensity for both the $PAF_{0.05}$-CNT and $PAF_{0.1}$-CNT anodes, providing evidence that the incorporation of PFSF monomer contributes to the improvement of ionic conductivity. Specifically, in Supporting Information S1: Figure S12e,f, the oxidation peak current (I_A) shows a positive correlation with the square root of the scan rate ($\nu^{1/2}$), whereas the reduction peak current (I_C) exhibits a negative correlation with $\nu^{1/2}$. The PAA-CB anode exhibited the lowest Li^+ diffusion coefficient (D_{Li}^+) during both lithiation and delithiation processes. However, the introduction of carbon nanotubes significantly increased the D_{Li}^+ of the PAA-CNT anode by one to two orders of magnitude, underscoring the profound impact of this three-dimensional conductive network on battery performance enhancement. The PAA-CB anode exhibited the lowest Li^+ diffusion

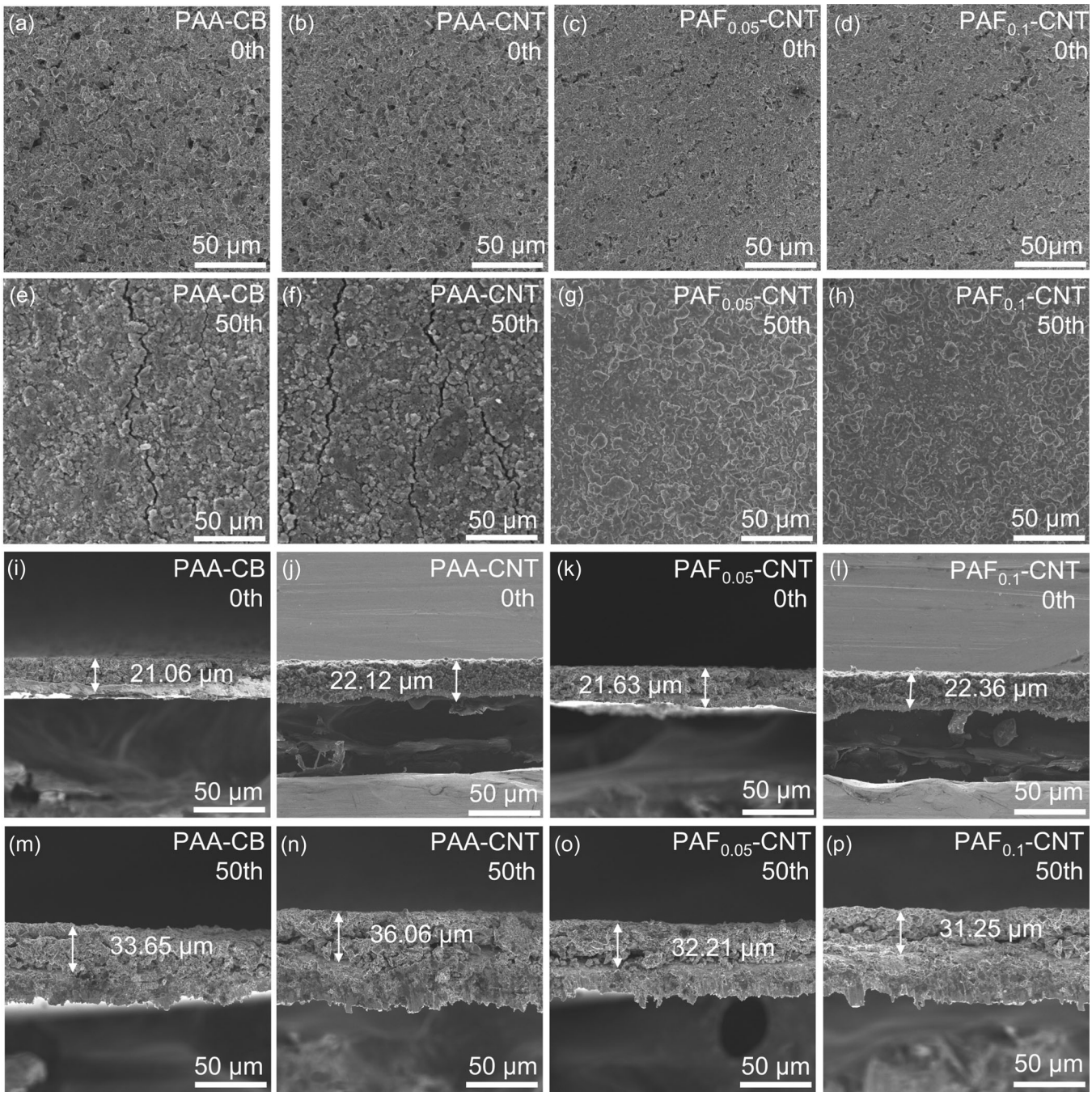

FIGURE 7 (a–h) SEM images of different anodes before cycling and after 50 cycles. (i–p) Cross-sectional SEM images of different anodes before cycling and after 50 cycles. CB, acetylene black; CNT, carbon nanotube; PAA, polyacrylic acid; SEM, scanning electron microscopy.

coefficient (D_{Li}^+) during both lithiation and delithiation processes. However, the introduction of CNT-NH_2 significantly increased the D_{Li}^+ of the PAA-CNT anode by one to two orders of magnitude, underscoring the profound impact of this three-dimensional conductive network on battery performance enhancement. Moreover, the incorporation of the PFSF monomer into the copolymer binder further improved the D_{Li}^+ of the PAF_x-CNT anode. This improvement can be attributed to the presence of the PFSF monomer, which is rich in perfluoropolyether side chains capable of participating in Li^+ coordination and transport through polar C-O-C bonds and -SO_2F functional groups. This facilitates the rapid diffusion of Li^+, contributing to the enhanced Li^+ conductivity observed in the PAF_x-CNT anode.[22]

Furthermore, to account for the variation in Li^+ diffusion kinetics during different charge and discharge stages, real-time analysis of Li^+ diffusion

kinetics during cycling was conducted via galvanostatic intermittent titration technique as illustrated in Supporting Information S1: Figure S14a,b. Initially, all four anodes showed comparable Li^+ diffusion coefficients (D_{Li}^+) due to insufficient activation of the SiO_x anode.[23] However, after five cycles, the D_{Li}^+ of PAA system anodes are significantly lower than that of PAF_x anodes and its D_{Li}^+ decreased compared with before the cycle. This is mainly due to the fact that the covalent bond of the SiO_x anodes with PAA as the binder cannot withstand the huge volume expansion, resulting in the covalent bond breaking, and eventually the particle crushing and subsequent loss of electrical contact. When PFSF monomer is introduced, the D_{Li}^+ of the PAF_x-CNT anode is two to three times that of the PAA-CB and PAA-CNT anodes. This further demonstrates the importance of the physical and chemical double-cross-linked three-dimensional conductive network of the PAF_x-CNT anode for buffering the volume expansion of SiO_x (maintaining the integrity of the electrode structure) and the involvement of polar C-O-C bonds and $-SO_2F$ functional groups in Li^+ coordination and facilitating Li^+ transport.

To further investigate the impact of the PAF_x binder on impedance and Li^+ diffusion processes in SiO_x anodes before and after cycling, the SiO_x anode underwent electrochemical impedance spectroscopy (EIS) analysis, measuring resistance before and after cycling. The equivalent circuit model depicted in Supporting Information S1: Figure S15 was used, with resulting resistances detailed in Supporting Information S1: Table S1. Initially, EIS curves (Supporting Information S1: Figure S16a) for all SiO_x anodes displayed a semicircle and a linear segment, representing charge transfer resistance (R_{ct}) and ion diffusion resistance (Z_w), respectively.[24] It is notable that the semicircle diameter of the PAA-CB anode exhibits a significant increase, with the charge transfer resistance (R_{ct}) measuring 178.60 Ω, surpassing that of other anodes. Conversely, the R_{ct} of the $PAF_{0.1}$-CNT anode is notably reduced, measuring only one-fourth of that observed in the PAA-CB anode. Postcycling (50 cycles), additional semicircles (R_{SEI}) emerged in the high-frequency region of EIS curves (Supporting Information S1: Figure S16b) for all SiO_x anodes. The $PAF_{0.1}$-CNT anode stood out with the lowest R_{SEI} (13.11 Ω) and R_{ct} (4.67 Ω), showcasing superior resistance characteristics both pre- and postcycling. This enhanced performance in the $PAF_{0.1}$-CNT anode can be attributed to the unique physicochemical double cross-linked structure derived from the $PAF_{0.1}$-CNT system, along with the rich-inorganic SEI induced by the sulfonyl fluoride group.

3 | CONCLUSION

The gradient hydrogen and covalent amide bonds formed by the $-SO_2F$ and -COOH of $PAF_{0.1}$ with the $-NH_2$ of CNT-NH_2 participate in the formation of physical and chemical double-crosslinked three-dimensional conductive networks, which give the SiO_x anode significantly enhanced performance. As shown in Figure 8, when the volume of SiO_x expands, the stress can be effectively dissipated through the stepwise dissociation of gradient hydrogen bonds with bond energies in a wide range (2.39–20.08 kcal mol^{-1}), maintaining the stability of the electrode structure and ensuring improve the long-term cycle stability of SiO_x anode. Simultaneously, the binder molecules possess a lower LUMO energy level compared to all solvent molecules. This characteristic predisposes them to preferentially undergo reduction on the anode surface, leading to the formation of inorganic components rich in Li_2O, Li_2SO_3/Li_2CO_3 and LiF. These components aid in reducing SEI impedance and enhancing the dynamics of Li^+ diffusion.

4 | EXPERIMENTAL SECTION

4.1 | Synthesis of $PAF_{0.1}$ copolymer binder

One gram of AA and either 0.05 g or 0.1 g of PFSF were separately placed into a three-necked flask. Subsequently, an appropriate amount of deionized water was added to dissolve the monomers to a mass fraction of 5 wt%. Nitrogen gas was then introduced into the three-necked flask for 30 min to eliminate oxygen. Finally, 5 mg of ammonium persulfate was added as a initiator for free radical polymerization. Under sealed conditions with nitrogen gas, the mixture was heated using an oil bath at 50°C for 8 h. Upon completion of the reaction, the solution was transferred to anhydrous ether, centrifuged, and subjected to repeated washing to obtain a colorless and transparent precipitate. This precipitate was then dried in a vacuum drying oven at 50°C for 24 h to obtain the PAF_x copolymer. The binders were labeled as $PAF_{0.05}$ and $PAF_{0.1}$, respectively, based on the mass ratio of PFSF to AA.

As shown in Supporting Information S1: Figure S17, the prepared $PAF_{0.1}$ copolymer has a precisely controlled molecular weight. The Mn and Mw of $PAF_{0.1}$ copolymer are 352,469 and 618,204 g mol^{-1}, and the relatively low polydispersability index is 1.75. In addition, ^1H and $^{19}FNMR$ spectra also supported the successful synthesis of $PAF_{0.1}$ copolymer (Supporting Information S1: Figures S18 and S19). In summary, free radical

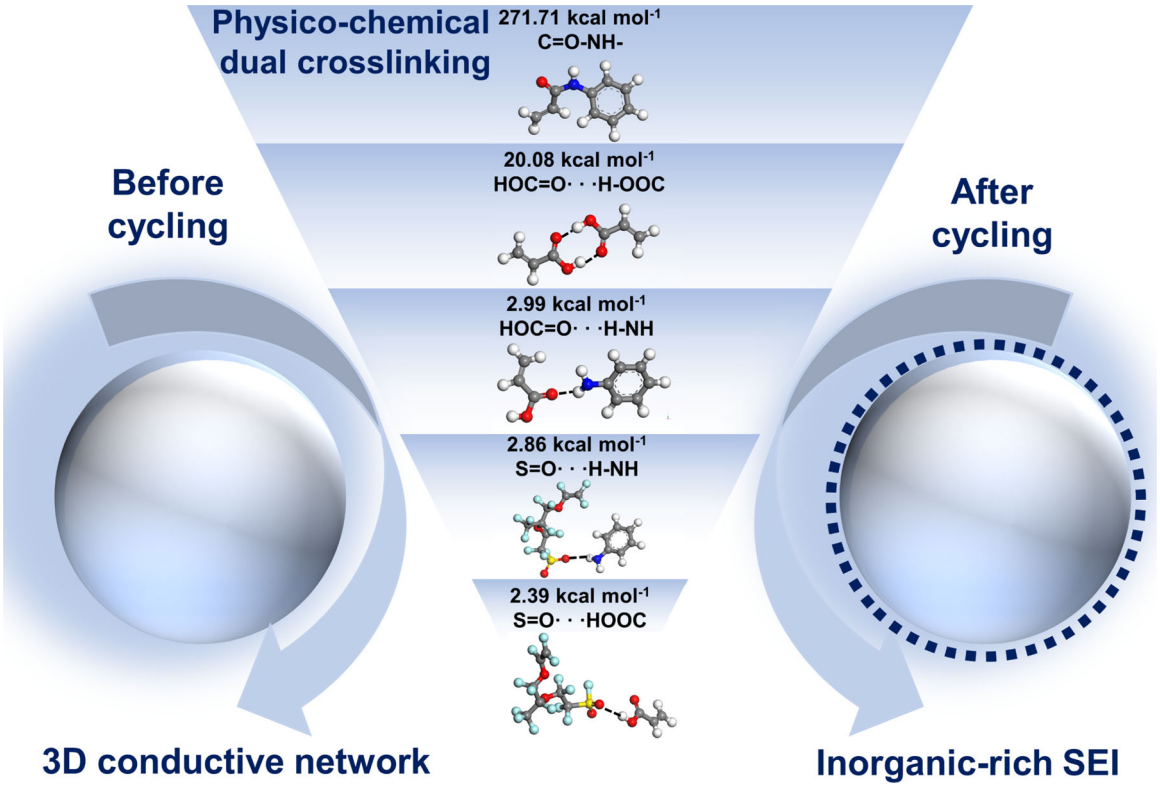

FIGURE 8 The mechanism of interaction between $PAF_{0.1}$ binder and SiO_x anode. 3D, three-dimensional; SEI, solid electrolyte interphase.

polymerization can precisely control the molecular structure of the polymer.

The materials characterizations, mechanical analyses, and electrochemical measurements were conducted following the methodology outlined in our prior work.[3b,21b]

AUTHOR CONTRIBUTIONS

Gen Chen and Gang Wu conceived the concept. Gang Wu and Yuanhang Gao designed and carried out the experiments. Yuanhang Gao conducted the theoretical calculations. Zheng Weng and Zhicheng Zheng assisted with carrying out the experiments and analyzing the data. Wenqiang Fan conducted verification and investigation. Gang Wu and Yuanhang Gao wrote the manuscript. Ning Zhang and Renzhi Ma reviewed and revised the manuscript. Gen Chen, Xiaohe Liu and Anqiang Pan supervised the whole project. All authors contributed to the discussion of the manuscript.

ACKNOWLEDGMENTS

Gang Wu and Yuanhang Gao contributed equally to this work. The authors acknowledge the financial support by National Natural Science Foundation of China (22379166), Natural Science Foundation for Distinguished Young Scholars of Hunan Province (2022JJ10089), Key Research and Development Program of Hunan Province (2023GK2015), and Central South University Innovation-Driven Research Programme (2023CXQD034). This work was supported in part by the High-Performance Computing Center of Central South University.

CONFLICT OF INTEREST STATEMENT

The authors declare no conflict of interests.

REFERENCES

[1] a) M. Armand, J. M. Tarascon, *Nature* **2008**, *451*, 652; b) J. W. Choi, D. Aurbach, *Nat. Rev. Mater.* **2016**, *1*(4), 16013; c) B. Scrosati, J. Hassoun, Y. K. Sun, *Energy Environ. Sci.* **2011**, *4*, 3287; d) B. Zhang, Y. L. Dong, J. R. Han, Y. J. Zhen, C. G. Hu, D. Liu, *Adv. Mater.* **2023**, *35*, 2301320; e) Y. Gao, G. Wu, W. Fang, Z. Qin, T. Zhang, J. Yan, Y. Zhong, N. Zhang, G. Chen, *Angew. Chem. Int. Ed.* **2024**, *63*, e202403668.

[2] a) S. Choi, T. Kwon, A. Coskun, J. W. Choi, *Science* **2017**, *357*, 279; b) J. Liu, M. Ben, A. Liu, J. Liu, S. Wang, J. Zhang, *Chin. Chem. Lett.* **2021**, *32*, 2914; c) Y. Yan, X. Zhao, H. Dou, J. Wei, W. Zhao, Z. Sun, X. Yang, *Chin. Chem. Lett.* **2021**, *32*, 910.

[3] a) S. Wu, Y. Yang, C. Liu, T. Liu, Y. Zhang, B. Zhang, D. Luo, F. Pan, Z. Lin, *ACS Energy Lett.* **2021**, *6*, 290; b) Z. Weng, S. Di, L. Chen, G. Wu, Y. Zhang, C. Jia, N. Zhang, X. Liu, G. Chen, *ACS Appl. Mater. Interfaces* **2022**, *14*, 42494; c) G. Wu, Z. Weng, J. Li, Z. Zheng, Z. Wen, W. Fang, Y. Zhang,

N. Zhang, G. Chen, X. Liu, *ACS Appl. Mater. Interfaces* **2023**, *15*, 34852.
[4] Y. X. Wang, X. F. Yang, Y. Yuan, Z. Wang, H. Z. Zhang, X. F. Li, *Adv. Funct. Mater.* **2023**, *33*, 2301716.
[5] a) B. Y. Jin, D. Y. Wang, J. Zhu, H. Y. Guo, Y. Hou, X. Gao, J. G. Lu, X. L. Zhan, X. J. He, Q. H. Zhang, *Adv. Funct. Mater.* **2021**, *31*, 2104433; b) Y. K. Jeong, J. W. Choi, *ACS Nano* **2019**, *13*, 8364; c) W. W. Zeng, L. Wang, X. Peng, T. F. Liu, Y. Y. Jiang, F. Qin, L. Hu, P. K. Chu, K. F. Huo, Y. H. Zhou, *Adv. Energy Mater.* **2018**, *8*, 1702314.
[6] a) X. X. Jiao, J. Q. Yin, X. Y. Xu, J. L. Wang, Y. Y. Liu, S. Z. Xiong, Q. L. Zhang, J. X. Song, *Adv. Funct. Mater.* **2021**, *31*, 2005699; b) Y. Wang, H. Xu, X. Chen, H. Jin, J. Wang, *Energy Storage Mater* **2021**, *38*, 121.
[7] J. Tang, J. Zhou, X. Duan, Y. Yang, X. Dai, F. Wu, *J. Energy Chem.* **2023**, *80*, 23.
[8] a) S. H. Di, D. X. Zhang, Z. Weng, L. Chen, Y. Zhang, N. Zhang, R. Z. Ma, G. Chen, X. H. Liu, *Macromol. Chem. Phys.* **2022**, *223*, 2200068; b) P. Li, G. Chen, N. Zhang, R. Ma, X. Liu, *Energy & Environmental Materials* **2021**, *4*, 72; c) H. A. Lee, M. Shin, J. Kim, J. W. Choi, H. Lee, *Adv. Mater.* **2021**, *33*, 2007460.
[9] a) B. Zhang, Y. Dong, J. Han, Y. Zhen, C. Hu, D. Liu, *Adv. Mater.* **2023**, *35*, 2301320; b) L. Hu, X. Zhang, P. Zhao, H. Fan, Z. Zhang, J. Deng, G. Ungar, J. Song, *Adv. Mater.* **2021**, *33*, 2104416.
[10] a) D.-Y. Han, I. K. Han, H. Y. Jang, S. Kim, J. Y. Kwon, J. Park, S. Back, S. Park, J. Ryu, *Energy Stor. Mater.* **2024**, *65*, 103176; b) Y. Wang, X. Yang, Y. Yuan, Z. Wang, H. Zhang, X. Li, *Adv. Funct. Mater.* **2023**, *33*, 2301716.
[11] K. Varaprasad, N. N. Reddy, S. Ravindra, K. Vimala, K. M. Raju, *Int. J. Polym. Mater.* **2011**, *60*, 490.
[12] C. Soykan, R. Coşkun, S. Kirbağ, E. Şahin, *J. Macromol. Sci. A* **2007**, *44*, 31.
[13] a) Y. Shen, J. Xi, X. Qiu, W. Zhu, *Electrochim. Acta* **2007**, *52*, 6956; b) I. Clara, R. Lavanya, N. Natchimuthu, *J. Macromol. Sci. A* **2016**, *53*, 492.
[14] K. P. Boroujeni, Z. Tohidiyan, A. Fadavi, M. M. Eskandari, H. A. Shahsanaei, *Chem. Select* **2019**, *4*, 7734.
[15] a) O. Sel, A. Soulès, B. Améduri, B. Boutevin, C. Laberty-Robert, G. Gebel, C. Sanchez, *Adv. Funct. Mater.* **2010**, *20*, 1090; b) M. Colpaert, M. Zaton, V. Ladmiral, D. Jones, J. Rozière, B. Ameduri, *Polym. Chem.* **2019**, *10*, 2176; c) B. Grabowska, S. Żymankowska-Kumon, S. Cukrowicz, K. Kaczmarska, A. Bobrowski, B. Tyliszczak, *J. Therm. Anal. Calorim.* **2019**, *138*, 4427.
[16] J. Xiong, J. Tao, K. Guo, C. Jiao, D. Zhang, H. Lin, Y. Chen, *Fibers Polym.* **2015**, *16*, 1512.
[17] M. Mokhtarifar, H. Arab, M. Maghrebi, M. Baniadam, *Appl. Phys. A Mater. Sci. Process.* **2017**, *124*, 21.
[18] S. Çavuş, G. Gürdağ, *Ind. Eng. Chem. Res.* **2009**, *48*, 2652.
[19] a) S. Pal, R. Mondal, S. Guha, U. Chatterjee, S. K. Jewrajka, *Polymer* **2019**, *180*, 121680; b) E. Su, O. Okay, *React. Funct. Polym.* **2018**, *123*, 70.
[20] P. Wang, H. Zhang, X. Nie, T. Xu, S. Liao, *Nat. Commun.* **2022**, *13*, 3370.
[21] a) H. Kim, K. Kim, J. Ryu, S. Ki, D. Sohn, J. Chae, J. Chang, *ACS Appl. Mater. Interfaces* **2022**, *14*, 12168; b) Z. Weng, G. Wu, J. Li, Y. Zhang, R. Zhang, N. Zhang, X. Liu, C. Jia, G. Chen, *Small Sci.* **2024**, *4*, 2300133.
[22] C. Sun, J. Liu, Y. Gong, D. P. Wilkinson, J. Zhang, *Nano Energy* **2017**, *33*, 363.
[23] X. Wan, C. Kang, T. Mu, J. Zhu, P. Zuo, C. Du, G. Yin, *ACS Energy Lett.* **2022**, *7*, 3572.
[24] a) Z. H. Li, Y. P. Zhang, T. F. Liu, X. H. Gao, S. Y. Li, M. Ling, C. D. Liang, J. C. Zheng, Z. Lin, *Adv. Energy Mater.* **2020**, *10*, 1903110; b) H. Liu, C. Li, H. P. Zhang, L. J. Fu, Y. P. Wu, H. Q. Wu, *J. Power Sources* **2006**, *159*, 717.

SUPPORTING INFORMATION

Additional supporting information can be found online in the Supporting Information section at the end of this article.

How to cite this article: G. Wu, Y. Gao, Z. Weng, Z. Zheng, W. Fan, A. Pan, N. Zhang, X. Liu, R. Ma, G. Chen, *Carbon Neutralization* **2024**;*3*:857–872. https://doi.org/10.1002/cnl2.158